Design and development of a low-cost angular sky luminance measurement system

Marshal Maskarenj, Rangan Banerjee, Prakash C Ghosh*

Department of Energy Science and Engineering, Indian Institute of Technology Bombay, Powai, Mumbai, 400076, India, e-mail: pcghosh@iitb.ac.in

Abstract

Energy efficient building design requires simulated assessment of overall performance through reliable models, taking into account the daylight variations along with other significant parameters such as ventilation, plug loads and occupant behaviour. A robust indoor daylight model applicable to locations across the globe needs to incorporate local variations of sky luminance on a spatial and temporal basis, and needs an affordable system for dynamic angular daylight measurement to be used as part of a wider distributed network. In the present work, a low-cost prototype based on Light Dependent Resistors for measurement of angular daylight luminance distribution is developed and analyzed. This device was used to capture the angular analog data for 221 sky segments (20 azimuthal x 11 altitudinal segments and Zenith). The analog data was further converted to luminance data, and the visualized data was compared with sky-dome photographs and also with simulated polar daylight maps for a few *Commission International de l'Eclairage* (CIE) skies. The repeatability of the experiment was assessed by comparing the luminance data for selected sky segments over multiple time-segments for consecutive days. Measured data was found to be an acceptable fit with the CIE-models over various time segments, validating the prototype.

Keywords: Building daylight modelling; Angular Sky luminance measurement; Daylight distribution; CIE sky model; Sky scanner

Highlights

- Design and Fabrication of novel low-cost prototype for angular measurement
- Experimental capture of sky luminance for an extended period covering three seasons
- Python-based open algorithm for data parsing and generation of sky-maps
- Analysis of spatial and temporal luminance variation for sky-segments over time
- Validation of the measured values using CIE skies as standard values

NOMENCLATURE

α	Azimuth angle of sky patch
α_s	Azimuthal angle of the Sun
a,b,c,d,e	CIE coefficients
A_{in}	Analog input data logged at the microcontroller
χ	Angular distance between Sun and sky-patch
f_χ/f_{Zs}	Scattering Indicatrix ratio
$\varphi_Z/\ \varphi_0$	Luminance gradation ratio
γ	Elevation angle
L_{in}	Luminance data at the sensor
L_z	Luminance at altitude Z
L_{Zen}	Luminance at Zenith

R_L LDR Resistance

Z_s Solar zenith angle

ABBREVIATIONS

CIE: *Commission International de l'Eclairage*

ERC: Externally Reflected Component

FOV: Field of View

HDR: High Dynamic Range

IDMP: International Daylight Measurement Program

IRC: Internally Reflected Component

LRTV: Light Ray Tracing and Visioning

LDR: Light Dependent Resistor

NRMSD: Normalized Root Mean Squared Deviation

PV: Photovoltaic

SC: Sky Component

RTC: Real Time Clock

RMSD: Root Mean Squared Deviation

SSLD: Standard Sky Luminance Distribution

SVF: Sky View Factor

1. Introduction

Among the major energy end-use sectors, buildings contribute a significant share. In the Indian context, commercial and residential buildings contributed to about 34.2% of the total energy use in 2012[1] with projections for 2022, 2030 and 2047 at 43.4%, 48.2% and 55.5% respectively. Among primary energy expense in buildings, electric space lighting accounts for a substantial share of total building energy consumption[2] (28% for residential buildings and 60% for commercial buildings in India[3]). Indoor daylight optimization can reduce the net energy usage by affecting two major segments: space heating/cooling and space lighting[4]. A combination of daylight prediction and measurement has been proposed towards minimizing the energy costs for space lighting[5], and scale models have been used for predicting the daylight factor and optimizing the building design[6]. Along with use in predicting illuminance distribution indoors through combination of daylight and artificial light, scale model was also reported in assessing light distribution during floodlighting through various distributed artificial light sources[7]. Validated package (DIVA) has been used to simulate the illuminance behaviour by changing dimensions of shading devices, and assessing four quantitative performance metrics: Mean Hourly Illuminance, Daylight Factor, Daylight Autonomy and Useful Daylight Illuminance[8]. Another metric proposed towards urban planning is the solar envelope concept—this aids in controlling maximum allowed building heights for regulating solar access to nearby structures [9,10]. Indoor light optimization involves the use of other avenues besides windows (side lights), as a combination of windows (side lighting), skylights (top lighting) and light guidance systems[11]. Daylight enhancement has been proposed using light guidance systems in buildings[12,13] and a reduction of about half the heat gain was reported[14]. Daylight in buildings serves an additional benefit: human eyes are evolved for highest sensitivity in visible spectrum. Natural light is crucial for human health and survival and has significant effect on human well-being, both physically and psychologically[15], and aids in patients healing process if adequately incorporated in hospital buildings, along with incorporation in schools, offices and commercial buildings for enhancing productivity and uplifting mood[16]. Being environmentally sustainable eventually leads to healthy communities and promotes economic sustainability[17]. To quantify the advantage achieved through modifications in the building design process, it is important to assess the year-round performance of the overall system: in terms of visual comfort as well as the net energy savings.

The cost of simulating annual building performance is less than metering physical systems, and this provides an incentive towards creating better indoor daylight simulation tools. Predicting daylight distribution indoors needs sky-luminance data, which can either be measured or modelled. Historically, sky-models have been used in the absence of measuring devices: the Lambertian uniformly-lit sky luminance model (1760) was accepted due to lack of measurement equipment and computational techniques[18]. With the invention of primary measurement techniques, the Lambertian model was replaced by the Moon-Spencer[19] model (1942) proposing a gradual change in sky luminosity across various altitude angles. While the Moon-Spencer model accounts for change in sky-luminance from zenith to horizon, this model does not consider the effect of the sun position, and assumes no variation across azimuthal orientations. The first robust model incorporating the effect of Sun position and scattering behaviour on sky-luminance distribution was proposed by Kittler in 1967[20], and the present Commission International de l'Eclairage (CIE) accepted model capable of simulating a most-probable set of skies was proposed in 2002[21]. However, a shortcoming in this robust global model, which is an industry standard for building energy simulation packages[22], is the need for incorporation of local aspects of angular luminance variation. The benchmarking of sky luminance distribution data quality may be done through predicting indoor light conditions; light distribution in the interiors from measurement-based models were reported to match with real conditions with good accuracy, but the predictions using CIE models underestimated the indoor lighting conditions[23]. This is due to the high smoothening of luminance distribution in the CIE model skies. To predict indoor daylight accurately, there is a need for sky models of higher accuracy, or large datasets of measured sky luminance values (for measurement based indoor predictions) at various locations. Devices built in accordance with CIE's IDMP (International Daylight Measurement Program) designed to capture sky luminance at discrete angular orientations cost about USD 35,000[1] as of July 2017. To address such issues as the costs involved in the commercial device, prototypes of Sky luminance measurement systems have been reported in literature. Few of these devices use image processing techniques to quantify the light distribution in the sky-vault: using a fish-eye lens on a camera[24], or using a spherical mirror to capture the hemispherical projection of sky-vault on a camera[25–27]. In our opinion, these techniques of capturing sky-distribution in a curved sky-vault over a fixed flat camera sensor works at angles closer to the zenith, but the projections near the horizon are captured as thin bands, thus diminishing the utility for vertical illuminance capturing. To counter the projection issue, the sensors need to face different orientations of the sky to measure the luminance distribution discretely. Literature reports devices with the capturing head turned at different spatial orientations, transmitting the light captured at the fore-optics to a spectroradiometer via optical fibers[28,29]. The spectral scan at the spectroradiometer quantifies the light intensity at varying spatial orientations across different wavelengths/colours, making the data useful for rendering purposes[28]. However, the use of spectroradiometers increases the cost of such devices, and the

[1] EKO MS-321LR quoted at about USD 37,500 including landing charges and taxes in July 2017

operational ruggedness needed for a long-term data capture in the exposed environment reduces the utility of such devices in developing countries. Thus, there is a need for low-cost devices, using low-cost sensors oriented at defined sky-angles for capturing the angular sky luminance distribution at various time-points. Such a device, in addition to enhancing the sky model through long-term data analysis, may also be used to predict indoor illuminance and be used as a centralized daylight control over a smaller region.

1.1. Background

The indoor daylight distribution is affected by the sky component "as seen" from inside a building as demonstrated in Figure 1(a). It is important to measure or predict the angular luminance distribution of the sky, since the luminance of the sky component as seen at a point in the room determines the achieved illuminance at that point in the indoors. The following segments describe the advances in measurement and modelling/prediction techniques for sky luminance distribution.

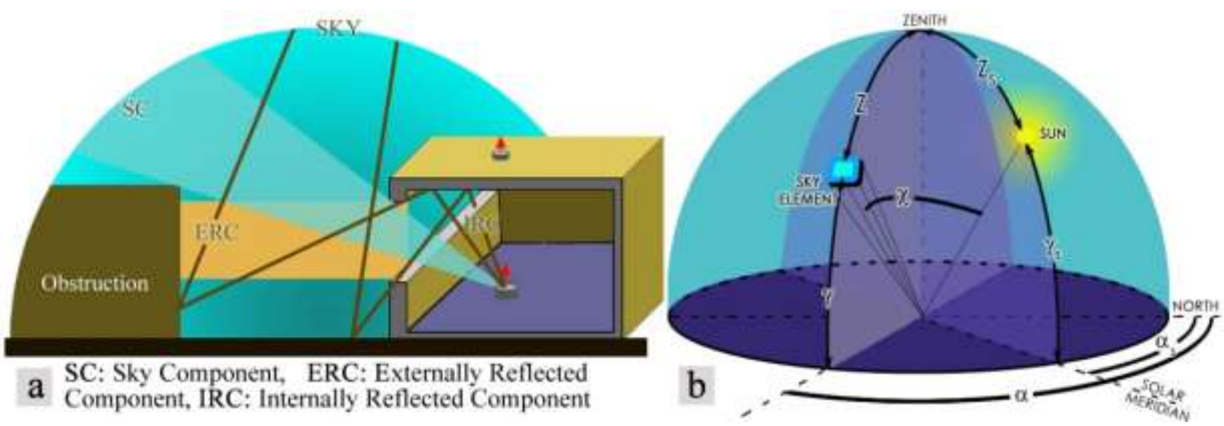

Figure 1: (a) Sky components 'as seen' from indoors, and (b) Various angles associated with sky elements and the Sun position

1.1.1 Evolution of sky models

The initial daylight models were proposed by Lambert (1760) and Bouguer (1762)[20]; while Bouguer suggested angular variation in sky illuminance, the lack of accurate measurement equipment restricted repeatability, and a uniformly lit Lambertian sky model was accepted. The Lambertian sky model wasn't contested till the early 1900s when a model was proposed by Schramm (1901) with a gradation factor: the variation in luminance across altitude from Zenith to Horizon. The Schramm model was modified by Moon & Spencer[19] and was accepted and recommended as the CIE sky model in 1942. This model proposed an angular distribution for any altitude (L_z) as a function of zenith luminance (L_{zen}) and zenith angle (z) as in Eq. 1.

$$\frac{L_z}{L_{Zen}} = \frac{1}{3}[1 + 2.\cos z] \tag{1}$$

The distribution followed a ratio of 1:3 from the horizon to the zenith, with zenith being the brightest and gradual darkening towards the horizon. The major flaw in this model was the oversimplification by ignoring the effect of the solar position.

The primary robust sky-model that incorporated the solar position was proposed by Kittler[30] (1967) and accepted as the CIE standard sky in 1996. This model proposed a correlation to predict the sky luminance at any elevation (γ) and azimuth (α), as a fraction of the zenith luminance as demonstrated in Eq. 2.

$$\frac{L_{\gamma\alpha}}{L_{zen}} = \frac{\left(1 - e^{-0.32/\sin\gamma}\right)(0.91 + 10e^{-3\chi} + 0.45\cos^2\chi)}{0.274(0.91 + 10e^{-3Z_s} + 0.45\cos^2 Z_s)} \tag{2}$$

Here L_{zen} is the zenith luminance, and Z_s is the solar zenith angle. The angular distance χ is a function of zenith angles of the Sun (Z_s), the sky-patch (Z), and the azimuthal angles of the Sun (α_s) and the sky patch (α) respectively as in Eq. 3.

$$\chi = \cos^{-1}\left(\cos Zs . \cos Z + \sin Zs . \sin Z . \cos(|\alpha - \alpha_s|)\right) \tag{3}$$

Figure 1(b) demonstrates the various angles in the Kittler's sky model presented above.

The CIE model 1996 was further advanced through evaluation of extensive data collection at Berkeley (1985-86) through a scanning system built by Pacific Northwest Laboratories. An advanced model was proposed incorporating gradation and scattering effects, and used tabulated coefficients to cover a wide range of sky-types with turbidity levels. This model through the coefficients classified all possible sky types into 15 most-probable skies[21]. The ratio of luminance of the arbitrary sky element with respect to the luminance at zenith is represented as a combination of gradation ratio (φ_Z / φ_0) and indicatrix ratio (f_χ / f_{Zs}) as demonstrated in Eq. 4.

$$\frac{L_{\gamma\alpha}}{L_z} = \frac{f(\chi).\varphi(Z)}{f(Z_s).\varphi(0^\circ)} \tag{4}$$

Scattering indicatrix ratio (f_χ / f_{Zs}) considers the luminance of a sky element based on its angular distance from the Sun, whereas the luminance gradation ratio (φ_Z / φ_0) relates the luminance of a sky element to the luminance at zenith.

For the luminance gradation function, the gradation at any sky element at angle Z from zenith is demonstrated in Eq. 5. By definition, the Z value at zenith is 0 degrees, as such, Eq. 6 demonstrates the luminance gradation function at the Zenith.

$$\varphi(Z) = 1 + a.\exp\left(\frac{b}{\cos Z}\right) \tag{5}$$

$$\varphi(0^\circ) = 1 + a.\exp(b) \tag{6}$$

The position of the Sun and the angle between the Sun and sky-element is included in the scattering indicatrix function that accounts for the change in Sun position as demonstrated in Eq. 7 and Eq. 8 for any sky element, and for zenith respectively.

$$f(\chi) = 1 + c.\left(\exp(d.\chi) - \exp\left(d.\frac{\pi}{2}\right)\right) + e.\cos^2\chi \tag{7}$$

$$f(Z_s) = 1 + c.\left(\exp(d.Z_s) - \exp\left(d.\frac{\pi}{2}\right)\right) + e.\cos^2 Z_s \tag{8}$$

The luminance at a certain azimuth/altitude can thus be measured as a fraction of the luminance at the zenith, and a sky-distribution map can be created by measuring/simulating for all discrete angles of altitude and azimuth. The position of the Sun affects Z_s and χ, and they can be calculated through the latitude angle, the day of the year and the time of day.

The coefficients a, b, c, d, and e in the CIE model are o get different sky distributions: The set of fifteen Standard Sky Luminance Distribution (SSLD) sets defined by CIE in 2003 to standardize all probable luminance patterns is demonstrated in Table 1. Six gradation(φ) coefficient (a,b) sets: (I, II, III, IV, V, VI); and six indicatrix(f) coefficient (c,d,e) sets (1,2,3,4,5,6) are defined to provide 36 standard skies, and 15 of which are selected based on most probable occurrences.

Table 1: Various sets of coefficients for functions φ (*a, b*) and f (*c, d, e*)

GRADATION SET	a	b	INDICATRIX SET	c	d	e
I	4.0	-0.70	1	0	-1.0	0.00
II	1.1	-0.8	2	2	-1.5	0.15
III	0.0	-1.0	3	5	-2.5	0.30
IV	-1.0	-0.55	4	10	-3.0	0.45
V	-1.0	-0.32	5	16	-3.0	0.30
VI	-1.0	-0.15	6	24	-2.8	0.15

These coefficients were defined based on an analysis of luminance scans done at Berkeley and supplemented by data from scans at Tokyo and Sydney in 1992[18,31].

Variation in the coefficients changes the luminance distribution from the zenith to the horizon, and at different distances from the solar position; and the cumulative effect of the gradation and indicatrix factors affects the overall luminance distribution as shown in Figure 2. The fifteen most-probable sky-types chosen by CIE[32] are listed in Table 2.

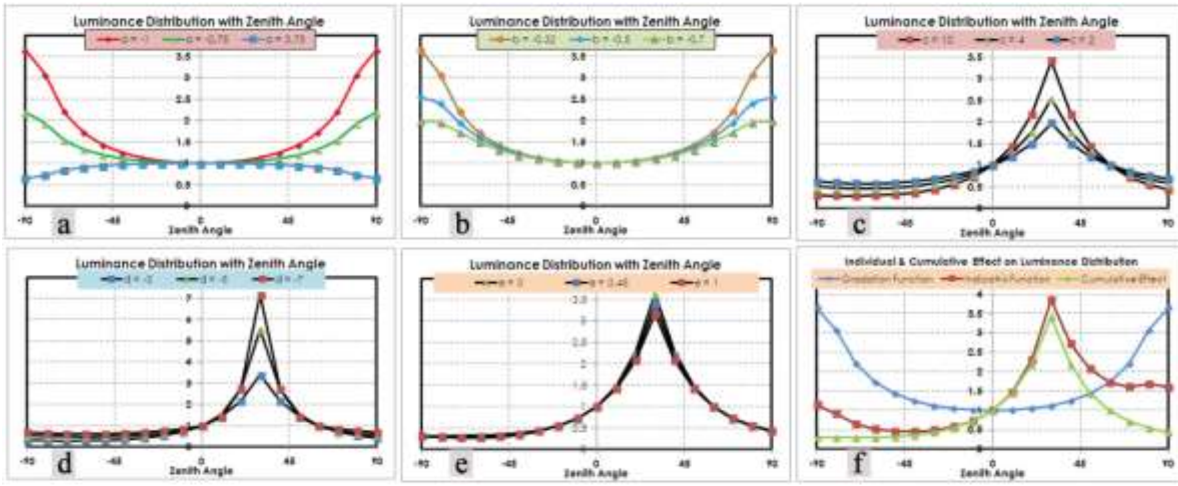

Figure 2: Change in sky luminance distribution as a function of various coefficients (a)-(e) respectively. (f) Cumulative effect of gradation and indicatrix factors on luminance distribution. (Sun position is at 30° with respect to Zenith)

Table 2: Standard coefficients for most probable CIE sky types

	φ( )	f( )	a	b	c	d	e	Description of Luminance Distribution
1	I	1	4.0	-0.7	0	-1.0	0.00	Overcast, steep luminance gradation towards zenith, uniform azimuthally: **CIE Standard Overcast Sky**
2	I	2	4.0	-0.7	2	-1.5	0.15	Overcast, steep luminance gradation & slight brightening near Sun
3	II	1	1.1	-0.8	0	-1.0	0.00	Overcast, moderately graded and azimuthally uniform
4	II	2	1.1	-0.8	2	-1.5	0.15	Overcast, moderately graded and slight brightening near Sun
5	III	1	0.0	-1.0	0	-1.0	0.00	Sky of Uniform Luminance
6	III	2	0.0	-1.0	2	-1.5	0.15	Partly Cloudy sky, No gradation, slight brightening near Sun
7	III	3	0.0	-1.0	5	-2.5	0.30	Partly Cloudy sky, No gradation, brighter circumsolar region
8	III	4	0.0	-1.0	10	-3.0	0.45	Partly Cloudy sky, No gradation, distinct solar corona
9	IV	2	-1.0	-0.55	2	-1.5	0.15	Partly Cloudy sky, Sun obscured
10	IV	3	-1.0	-0.55	5	-2.5	0.30	Partly Cloudy sky, bright circumsolar region
11	IV	4	-1.0	-0.55	10	-3.0	0.45	White blue sky with distinct solar corona
12	V	4	-1.0	-0.32	10	-3.0	0.45	**CIE Standard Clear Sky,** low illuminance turbidity
13	V	5	-1.0	-0.32	16	-3.0	0.30	**CIE Standard Clear Sky,** polluted atmosphere
14	VI	5	-1.0	-0.15	16	-3.0	0.30	Cloudless turbid sky with broad solar corona
15	VI	6	-1.0	-0.15	24	-2.8	0.15	White-blue turbid sky with broad solar corona

To encourage daylight measurement, locations were identified worldwide for logging daylight measurement[33] in 1991. As of 1994, the IDMP included 48 stations logging the data globally, with three classes of data measurements depending on the complexity of data measurement: from logging just the global illuminance and irradiance at the basic stations to measuring more complex data through scanners at research stations[20]. More non-IDMP measurements were conducted at Bahrain, Japan, Kuwait and Portugal[33], that measured Global, Diffuse and Beam

Irradiance between 1982-1990 (Portugal) to 2000-2002(Bahrain). However, most of the original IDMP stations now have ended their operations, owing to cost of operations and local support.

The CIE skies have been validated through measurements [34–40] at few locations, and the CIE sky-ratio models have been extended from luminance to irradiance distribution predictions for PV modules at inclined planes[41]. Further calculation based enhancements have been demonstrated for urban environments where the sky is not directly visible due to dense construction; the calculation of solar heat gain and daylight intrusion through vertical fenestration was demonstrated for standard CIE skies[42], and since the amount of interior daylight depends on the light reaching the facades, a calculation procedure was proposed for assessing the luminance on a vertical plane[43]. Real-time classification of the sky into CIE skies through feedback loop analysis of sky luminance distribution was demonstrated towards optimal use of indoor lighting[44]. Machine learning approach using classification tree algorithm has been trained to identify sky-types through available metrological data: sky luminance distribution measurements conducted at Hong Kong between 2004-05 using EKO MS-301 LR were compared with CIE model-skies using RMS approach, and the frequency of occurrence for various sky-types were fed as training sets, along with input parameters available in metrological weather data such as normal irradiance, wet bulb temperature, dew point temperature, turbidity, clearness index, etc [45] The machine-learning approach was reported to correctly predict 83.2% skies into overcast, intermediate and clear sky types using available metrological data, and had a precision of 62.7% in classifying into the specific CIE sky-type as deduced using frequency of occurrence approach through actual measurements .

Presently, the CIE models are being used in simulations; with the CIE overcast sky and CIE standard sky being the choice for architects using standard design packages[22]. However, the smoothness of the modelled data across various spatial positions can lead to underestimation of indoor daylight distribution. Measurement-based models for indoor light distribution have higher merit than model-based prediction, thus there is a need for sky-luminance measurement systems.

1.1.2 Advances in sky luminance measurement techniques

Measurement systems are the basis of analytical models. The accuracy of the measurement systems has advanced over the years, leading to the more accurate models for predicting daylight distribution. One major issue with the accuracy of luminous distribution measurement is the great diurnal variation in the intensity of ambient illumination; the ambient brightness during the day is about 1,000,000 (night with the moon) to 100,000,000 (night without moon) times higher than that at night[46]. There are also discrepancies near the circumsolar region from the rest of the sky clubbed with high unpredictability in cloud distributions, and this needs better measurement devices. Initial techniques for sky measurement used a pyranometer to analyze the global horizontal irradiance. After the development of spot luminance meters, the directional luminance could be measured by pointing the device in any direction, and the diffuse horizontal luminance could be captured. In field of irradiance measurement, devices using shadow ring for irradiance measurement[47], sky imaging[48] and image processing protocols[49] have been reported. The amount of clear unobstructed sky visible to such a measuring device may be denoted by the Sky-view factor (SVF), a dimensionless value that represents the proportion of unobstructed sky visible at any point. For sparse locations, the SVF approaches 1 and the wide angle of exposure offered by the sky-dome challenges the capturing capability of the sensors. To address the issues in capturing such wide angles, an image processing approach was reported involving a digital camera mounted with a fisheye lens for capturing wide angles[24]. Another approach involving projecting the sky-dome on the spherical mirror was reported[25]. This hemispherical sky projection concept was used to develop a Light Ray Tracing and Visioning (LRTV) device[27], and employed to identify sky view factors for horizontal[26] and vertical planes[25]. The image processing approach involved the polar transformation of the RAW photos taken from a calibrated camera[27] and quantification of the luminance distribution through discrete angles. Commercial systems rotating sensors based on IDMP recommendations have been developed: most papers involving commercial designs report the use of Japanese EKO [50–53] or German PRC Krochmann systems[54,55].

While quantifying discretely measured sky-luminance distribution, it is important to identify the sky-discretisation technique. An approach for scanning the sky-dome using luminance meters was proposed by Tregenza, dividing the hemisphere into equal sized patches[56]. An optimal subdivision into 8 bands and 151 patches was recommended, with an angular width about 12 degrees at each band centre. Owing to difficulties in designing measurement devices with 28 and 32 patches in sixth and eighth patch as proposed in Tregenza's calculations, a slightly modified design with 24 and 30 patches on the sixth and eighth band was selected for the commercial EKO and PRC Krochmann scanning systems, which use a single probe to scan the 145 sky patches in a pattern. Few works have demonstrated original sky-scanning techniques[28,29] as an alternative to commercial systems, or substitute for scanning through image processing of fisheye High Dynamic Range (HDR) photographs of the sky-dome[24], but used a similar subdivision protocol while analytically assessing the sky luminance in various parts of the sky hemisphere. A novel scanner built with a single rotating probe reports an 81-patch subdivision with 5-bands having 1, 6, 16, 24 and 32 patches respectively[28]. Most sky-discretisation protocols in literature-based designs and in adapted commercial systems report a subtended angle of about 12 degrees. However, a separate study observed a higher inaccuracy for sky subdivision if the field of view (FOV) exceeded 10°, and an optimum FOV based on accuracy and scan time was proposed at 5°[57].

Low cost approaches using flat sensors and curved projections using mirrors or lenses fall short at angles approaching horizon, while reported designs using rotating heads facing defined sky angles use costly and fragile equipment like spectrophotometer that may not be useful in rugged environmental conditions for long term data capture. Commercial device built using CIE IDMP recommendations presents the challenge of affordability (about USD 37,500), making it out of range for researchers in developing countries.

2. Design of the angular luminance measurement system

The primary focus of this work was to build a device with low-cost sensors facing defined sky positions, aimed at measuring the luminance distribution of daylight under real sky. It was important to capture sky-luminance in the range suitable for human spectral sensitivity through spatial and temporal intervals: capturing the luminance at discrete positions at fixed time intervals. Human eyes, through an evolutionary process, are best suited for daylight— visible light between 400-700 nm with the highest sensitivity towards the yellow-green zone around 550 nm. To match the spectral response of the human eyes, LDRs were chosen as photosensitive device for quantitative measurement of variation in sky luminance because of their similar spectral response as human eyes[58], low noise from the infrared region, high response to luminous intensity and low unit cost. To discretise into defined positions, the sky was divided into 221 segments—20 azimuthal and 12 altitudinal segments, with an LDR representing each altitudinal position through exposure control. The azimuthal segments were catered to by varying the device orientation on a vertical axis using a stepper motor controlled by a microcontroller.

Since the zenith remains unchanged through all azimuthal variations, the total subdivision of the sky-vault was done in 221 patches (20x11 + Zenith).

2.1 Design schematics

Arduino Mega 2560, an open-source microcontroller by Arduino CC was chosen for controlling the mechanical rotation of the device, and for storing the LDR-generated data with timestamps. Each of the 12 LDRs was a part of a voltage divider network (VDN), the change in resistance owing to variation in light intensity resulted in a potential drop, which was measured at the microcontroller. Moreover, the data inputs from the timer and the motor control were done at the microcontroller as demonstrated in Figure 3.

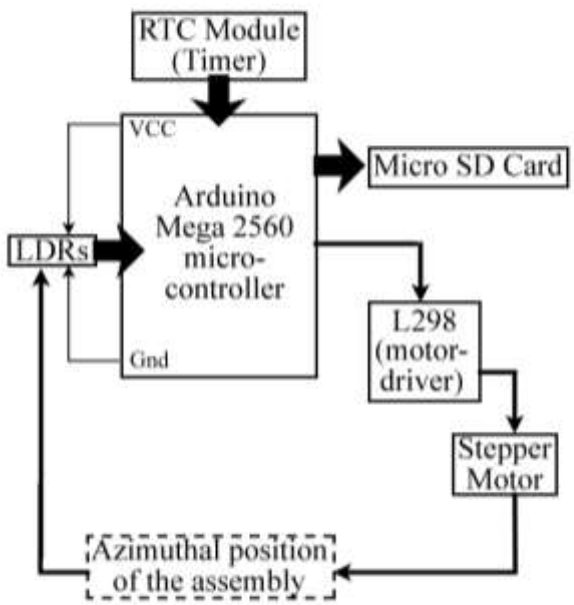

Figure 3: Data acquisition scheme of the measurement and logging system

2.2 Sensor calibration

LDRs were pre-calibrated for their analog-in values as a function of the light intensity. Using a HTC-LX103 digital lux-meter, the Analog-in values (0-1023) at the Arduino were plotted against the lux values generated at the same location for the lux-meter as the LDR. The calibration was performed for three light sources to capture the entire intensity spectrum: white LED for low intensity, a 100W Incandescent bulb for mid-range and exposure to Sunlight from early morning until peak noon for high intensity range. For the LED and bulb, light intensity was varied by moving the source vertically upwards on a light-stand, as demonstrated in Figure 4. The representative calibration curve is also demonstrated.

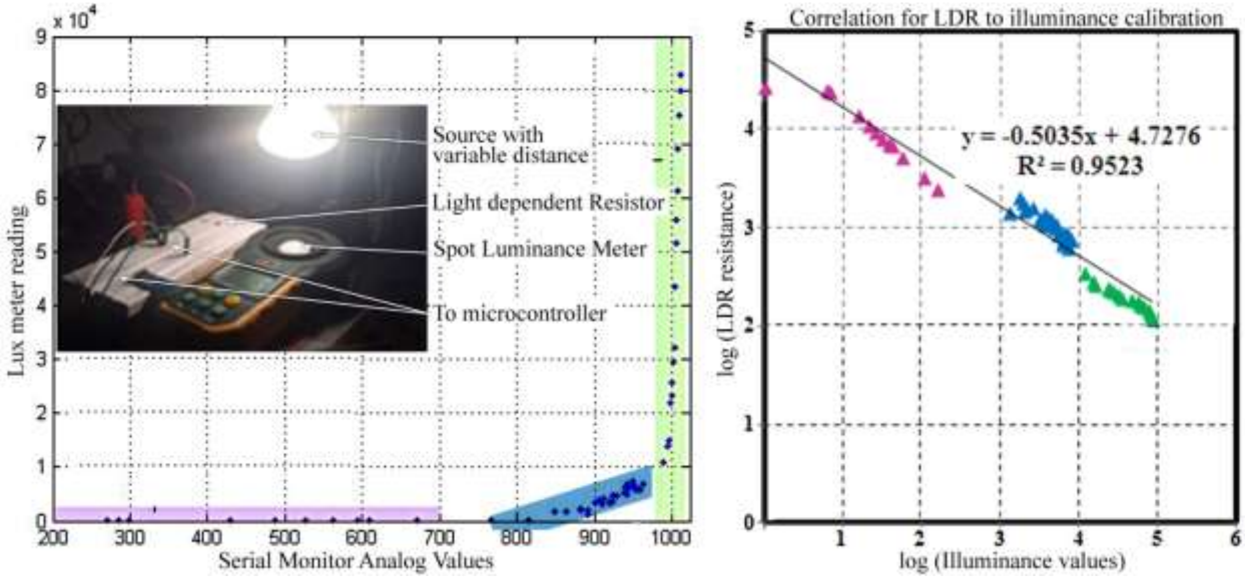

Figure 4: Calibration of LDR analog value with light intensity using lux-meter

The analog value was converted to LDR resistance (R_L), and a plot of log(R_L) with log(luminance value) for the presented sensor found the following linear correlation with R^2 value at 0.9523 demonstrated in Figure 4:

$$L_{in} = \text{antilog}_{10}\left[9.3815 - 1.986\,\log_{10}\left(10{,}000 \text{ x } \left(\frac{1023}{A_{in}} - 1\right)\right)\right] \qquad (9)$$

Through correlation as demonstrated by a representative correlation in Eq. 9, the analog values at the microcontroller (A_{in}) were converted to corresponding lux values (L_{in}) during data processing.

2.3 Data capture and storage

The device has twelve LDRs mounted at 7.5° interval, with two sets of six LDRs placed azimuthally opposite. To control the aperture, tubular casings were used to avoid overexposure and sensitivity to light difference over wider angle as demonstrated in Figure 5.

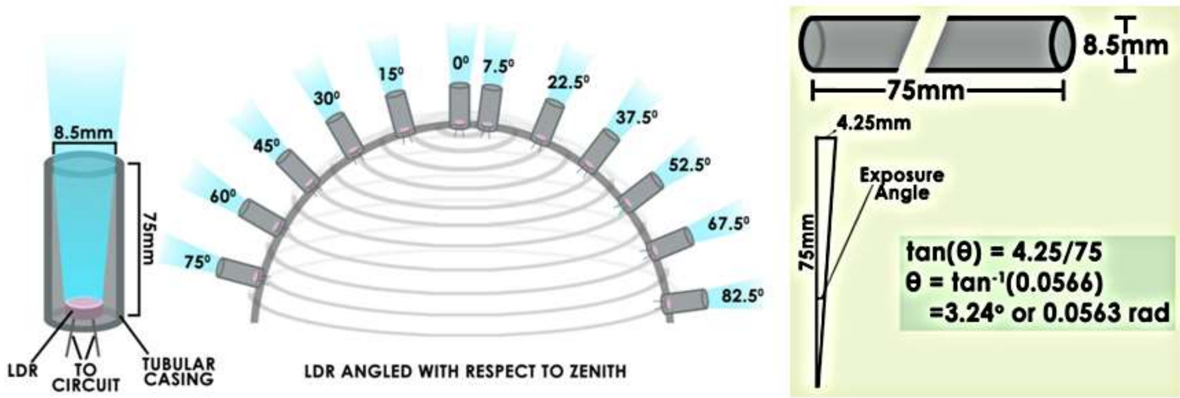

Figure 5: LDR positioning and exposure control

Before saving the data along with timestamps generated via a RTC chip onto the SD card, the primary data was transposed as demonstrated in Figure 6.

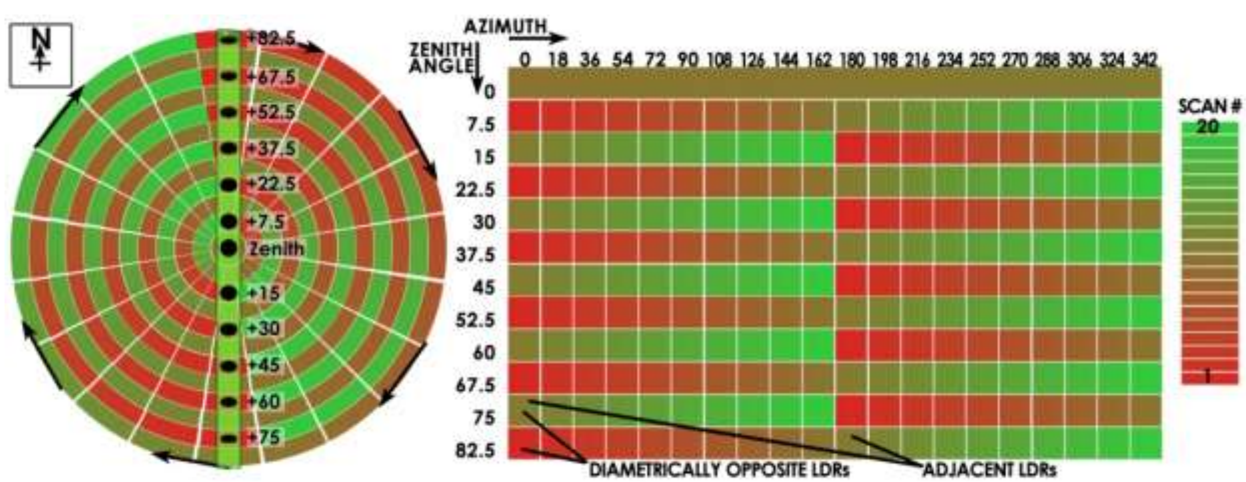

Figure 6: Scan motion of the assembly and data saving protocol on the SD Card from Scan1 till Scan20 for each LDR

2.4 Mechanical design

The frame was fabricated based on the size of the sensor, to avoid space conflict between the LDRs at the Zenith and Z+7.5° positions. LDRs were mounted at twelve altitudinal positions: at Zenith, Z+7.5°, Z+15° and consecutively till Z+82.5°. The D-shaped frame measuring 42 cm at the base was rotated to orient the sensors into defined azimuthal positions in a step-wise manner. The assembly was turned across 18° azimuth; the experimental design of the setup is demonstrated in Figure 7.

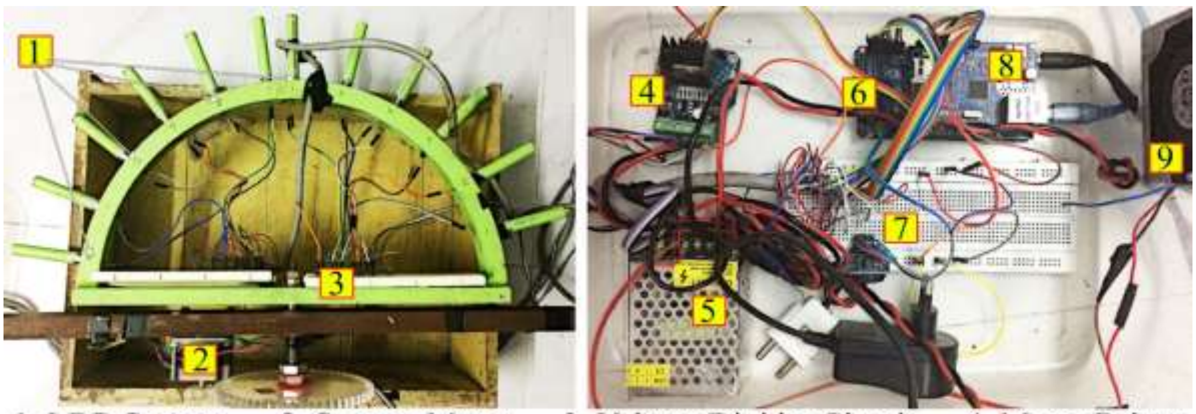

1. LDR Sensors 2. Stepper Motor 3. Voltage Divider Circuit 4. Motor Driver
5. SMPS 6. Arduino Microcontroller 7. RTC 8. SD Card Shield 9. Exhaust Fan

Figure 7: Sky luminance measurement prototype with the data acquisition

Due to the weight of the rotating assembly, a heavy duty high torque stepper motor (1.8° per step) was used in a dual phase mode, with a 1:6 gear mating through designed involute gears designed to supplement extra turns for the required torque. After twenty azimuthal steps of 18° each complete rotation, the frame was reoriented to its original position. Silicon rubber was used to minimize vibrations between the metal frame, acrylic-gears and other rotating parts.

2.5 Fisheye sky-photographs.

To obtain sky photos of the hemisphere for visual comparison and assessment, Google Street View app was used to capture and stitch 72 photos captured at various 3-dimensional angles, to generate a polar panorama on an iPhone 5S. The upper half of the panorama was transposed to polar coordinates using Polar Coordinate Distortion Filter on Adobe Photoshop CS3 (Filter > Distort > Polar coordinates) as demonstrated in Figure 8. This was repeated every 15 minutes, to synchronize with data capture from the device.

Figure 8: Generation of fisheye image through polar coordinate conversion for two tested locations: a) Urban Location: Hostel 1, IIT Bombay; and b) Sparse Location: Open Air Theater, Students Activity Center, IIT Bombay

3. Experimental measurements and analysis

Mumbai, India is located at (~19.1°N, 72.9°E) and is a coastal city with a tropical savanna climate. The monsoons last from early June till mid-October, with peak around July. The experimental design included three distinct seasonal phases: pre-monsoon (mid-May), mid-monsoon (July-Aug) and post monsoon (Oct-Nov). Luminance data for May 19 (Day 139) was chosen as representative pre-monsoon set with scant clouds and July 28 (Day 209) as mid-monsoon set with highly cloudy/overcast behavior. Both representative days have very similar declination angle (N19°38’ and N19°08’ respectively) since they are almost symmetrically equidistant from equinox day, thus the Sun path is very similar for these two although the sky-type is very different.

To assess the reliability of measured data in absence of a standard angular luminance measurement device, extensive analyses were conducted on the captured data. A qualitative analysis was done through data visualization: the calibrated measurements for spatial luminance distribution were used to generate sky-maps at fixed intervals and compared with polar fisheye sky-photographs. A quantitative assessment was -subsequently conducted based on temporal variation for specific sky-positions: the luminance variation at few fixed sky positions was analyzed through time, based on the sun-path and sun-distance for the sky patches. Statistical analysis of the captured data and predicted luminance for specific positions at different time-points for various CIE skies provided the reliability in measurements. Experimental repeatability was established by processing data of multiple consecutive similar days in November with similar clear sky.

3.1 Spatial validation

Device was run in continuous mode with sampling rate of one set each 15 minutes. Data from dusk to dawn was discarded based on timestamps. By parsing through the raw set of 20x12 data points for each set, the python script interpolated it to 360x90 data points and converted it from cylindrical to polar array. Luminance plots were generated and saved for each time point for visual assessment. A separate script processed the zenith luminance and the diffuse horizontal illuminance values captured from an exposure-controlled spot luminance meter, and based on the time stamp, the solar position was evaluated: all 15 model CIE skies were generated and the modeled angular luminance data for each time stamp for each sky type was saved for standard comparison. Figure 9 demonstrates the spatially-separated angular luminance distribution comparison for few selected time-stamps; between measured distribution, modeled skies and sky photographs.

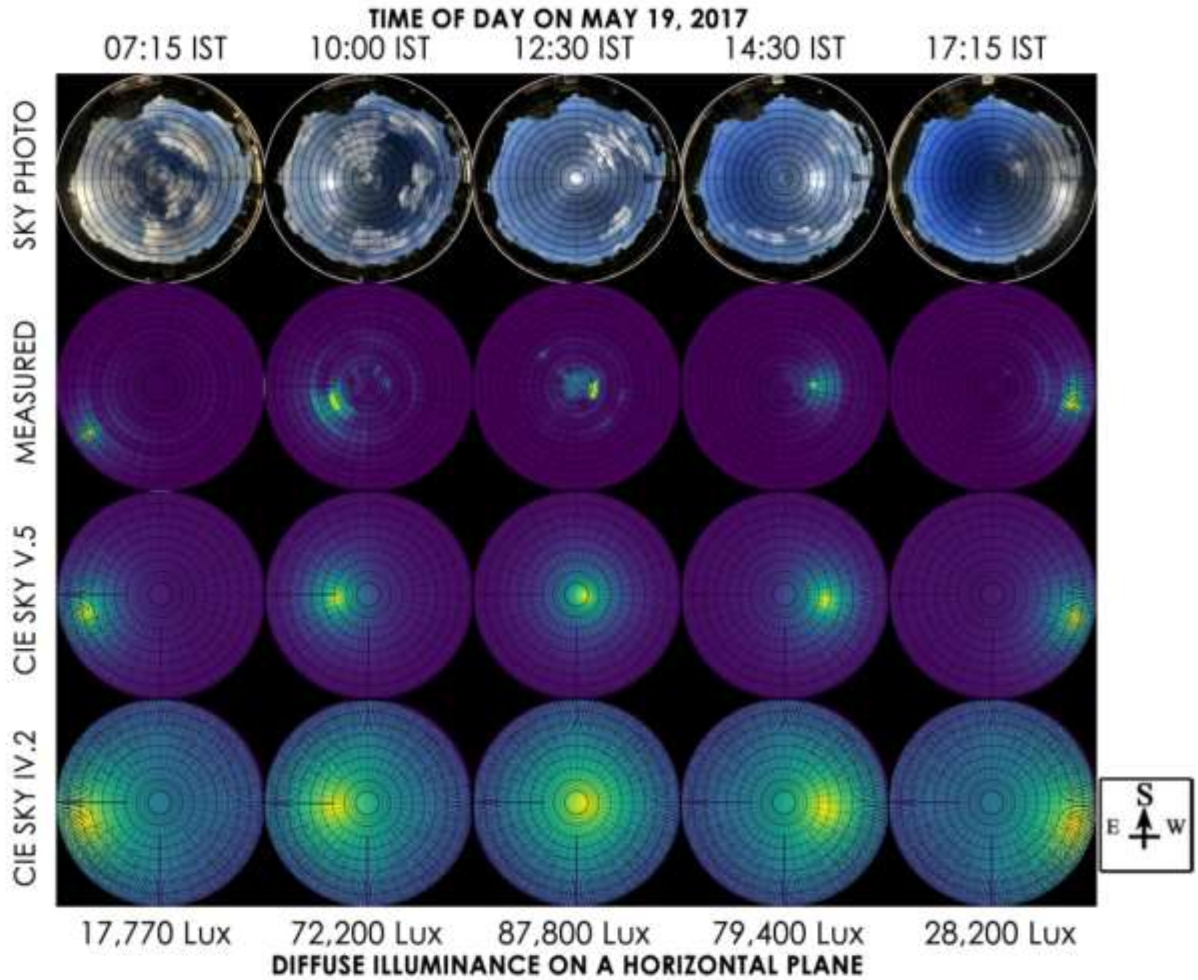

Figure 9: Comparison of measured and photographed sky-hemisphere with CIE mode skies at few discrete time-points

3.2 Temporal validation

Sky patches at few selected orientations were chosen and their luminance monitored as demonstrated in Figure 10. The luminance of patches near the Sun-path peaked higher at the appropriate time with the closest Sun-approach as compared to patches farther apart. As observed in Figure 10, the patch at 36°/45° orientation facing north-north-east, peaked in the morning, while 270°/45° showed a higher peak in the evening, owing to closer proximity to Sun-path.

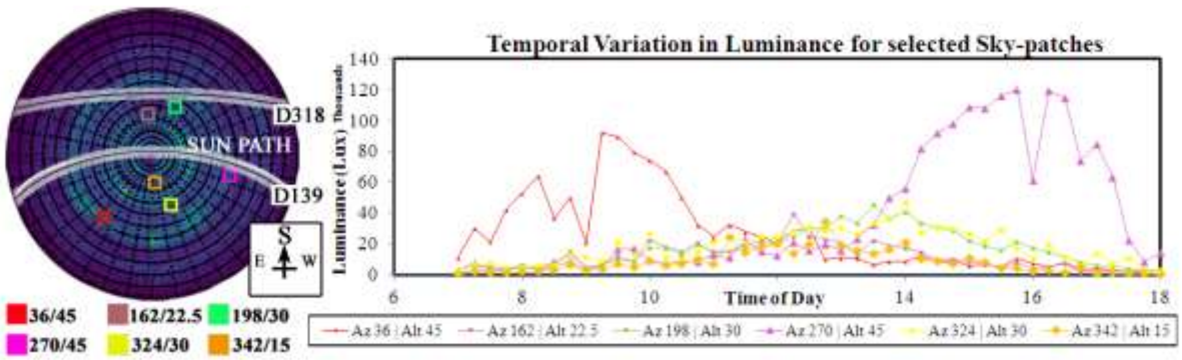

Figure 10: Variation in measured luminance of various sky patches at different times of the D139 (19 May)

Other patches closer to the due south (162°/22.5° and 198°/30°) or the due north (324°/30° and 342°/15°) peaked in luminance close to Solar noon, although their individual peaks were found much lower.

3.3 Comparison of similar days

To compare data repeatability, few selected orientations (same as those represented in Figure 10) were analyzed over a span of consecutive similar days during November, through 14-17 November 2017. The repeatability is demonstrated in Figure 11. Since 198°/30° patch falls very close to the Sun-path of D318 (Nov 14), with D319 passing through the patch, a high luminance induced by the direct Sun is seen for second day of the data; also patch 162°/22.5° falls close to Sun-path in November and experiences high luminance. Other four representative patches demonstrate lower luminance through the day.

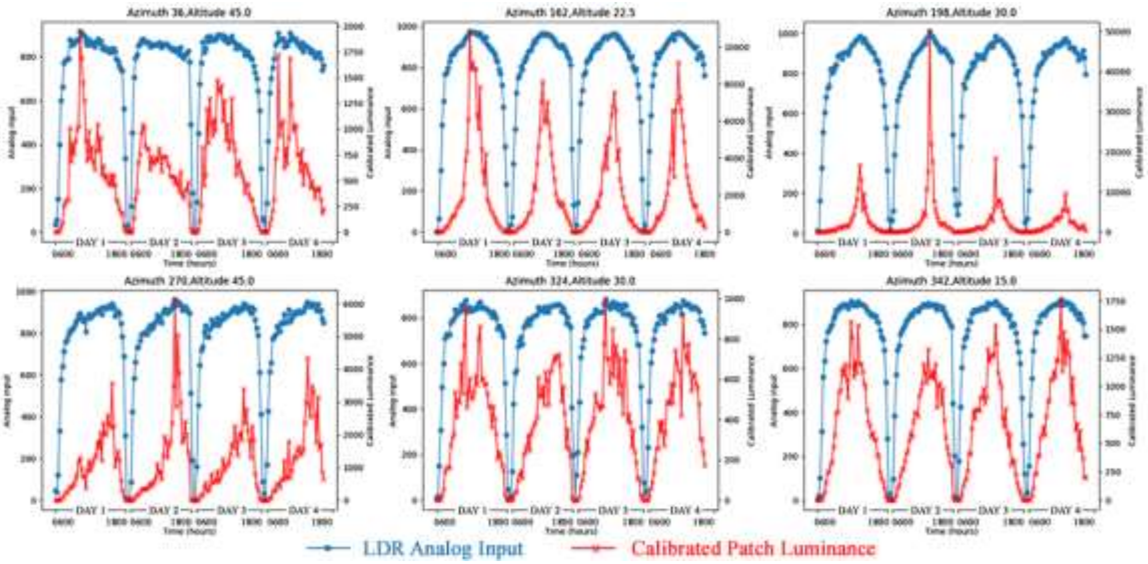

Figure 11: Luminance from selected patches demonstrating repeatability through the experimental duration in post-monsoon clear sky conditions (Nov 14-17, Day 318-321)

3.4 Comparison with standard skies

The diffuse horizontal illuminance and zenith luminance data was measured with a luminance meter, and the solar position at the respective timestamps was assessed using solar geometry. With CIE coefficients for 15 sky types, the CIE skies were generated for those timestamps in Python using MatPlotLib module, and compared with the sky photos and measured sky-luminance maps. Moreover, the temporal variation in measured luminance for selected sky positions was compared with respective variation in CIE modelled skies for the experimental duration.

A comparison of temporal variation of experimentally measured luminance of sky-patches with the luminance predicted using CIE skies was drawn, and Figure 12 demonstrates a comparison of experimental data with closest CIE sky. The deviations in the measured data with the CIE sky predictions could partially be attributed to the clouds.

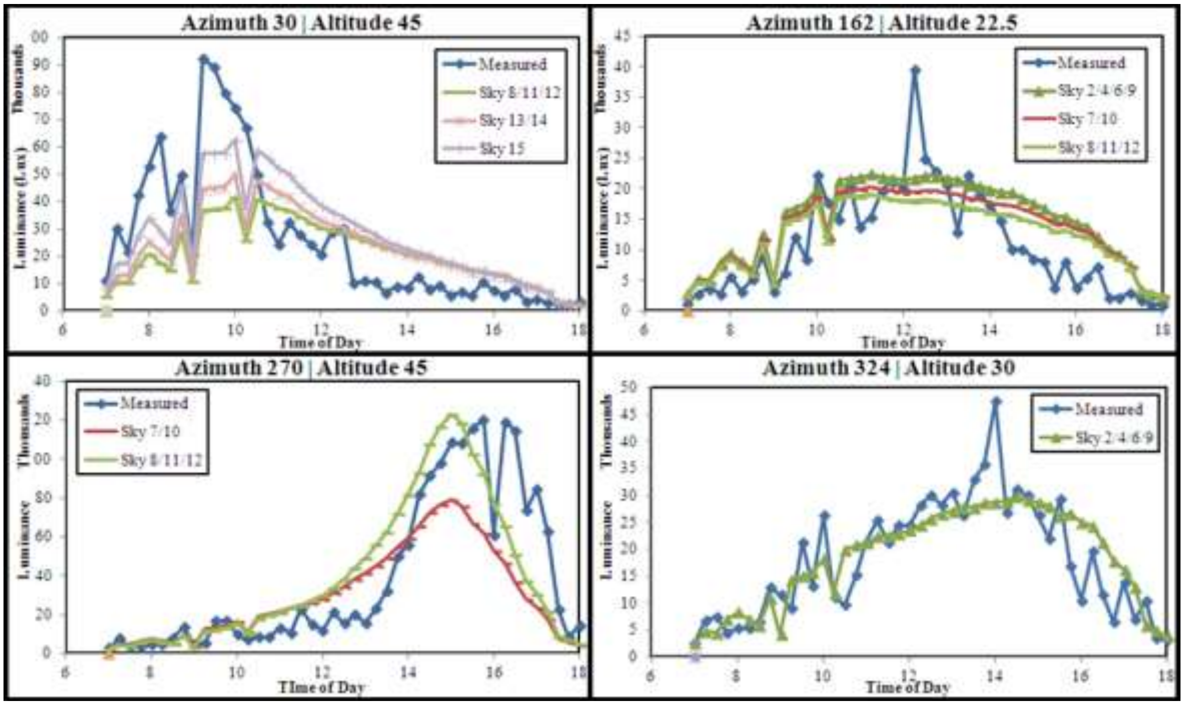

Figure 12: Comparison of measured experimental data with closest CIE skies at selected patches

To analyze the error in experimental data with respect to model skies, the Root Mean Squared Deviation (RMSD) and Normalized Root Mean Squared Deviation (NRMSD) were calculated to assess the closest CIE sky for the measured data as follows:

$$\text{RMSD} = \sqrt{\frac{\sum(\text{Lux}_{\text{measured}} - \text{Lux}_{\text{model sky}})^2}{\text{n}}} \qquad (10)$$

Where $\text{Lux}_{\text{measured}}$ and $\text{Lux}_{\text{model sky}}$ are the luminance values from measured data and from modeled dataset for a given sky-patch through the day, and ‘n’ is the number of data points in each. RMSD is normalized by dividing with the maximum change (maximum value – minimum value) in the dataset as follows:

$$\text{NRMSD} = \frac{\text{RMSD}}{\text{Lux}_{\text{model,max}} - \text{Lux}_{\text{model,min}}} \qquad (11)$$

Table 3 demonstrates the comparison of captured data with CIE model skies at the selected patches.

Table 3: RMSD and NRMSD for luminance comparisons: selected sky patches over various CIE model skies.

	Sky 2/4/6/9	Sky 7/10	Sky 8/11/12	Sky 13/14	Sky 15
RMSD	($x10^3$)				
36/45	23.8	21.9	19.8	17.6	15.5
162/22	6.1	5.6	5.4	5.3	5.2
270/45	34.2	26.1	21.6	28.4	45.9
324/30	5.7	6.7	8.4	11.1	17.1
NRMSD	(normalized)				
36/45	0.807	0.646	0.488	0.363	0.251
162/22	0.289	0.296	0.304	0.306	0.290
270/45	0.764	0.337	**0.179**	**0.170**	0.206
324/30	0.207	0.225	0.245	0.269	0.307

3.5 Comparing measured distinct sky-types

Day 209 has a solar declination angle similar to Day 139 (N19°23' ± 15'), yet these represent days with different sky-types for Mumbai: D139 (May 19) represents pre-monsoon with scant clouds while D209 (July 28) falls in the middle of monsoons, with overcast sky through the day. A comparison between the measured data for various time-points on these representative days ($[Lux_{T,139} - Lux_{T,209}]|_{all\ patches}$) is demonstrated in Figure 13: the spatial orientations close to the Sun have greater luminance on the clear day, but those away from the Sun have lesser luminance as compared to an overcast day.

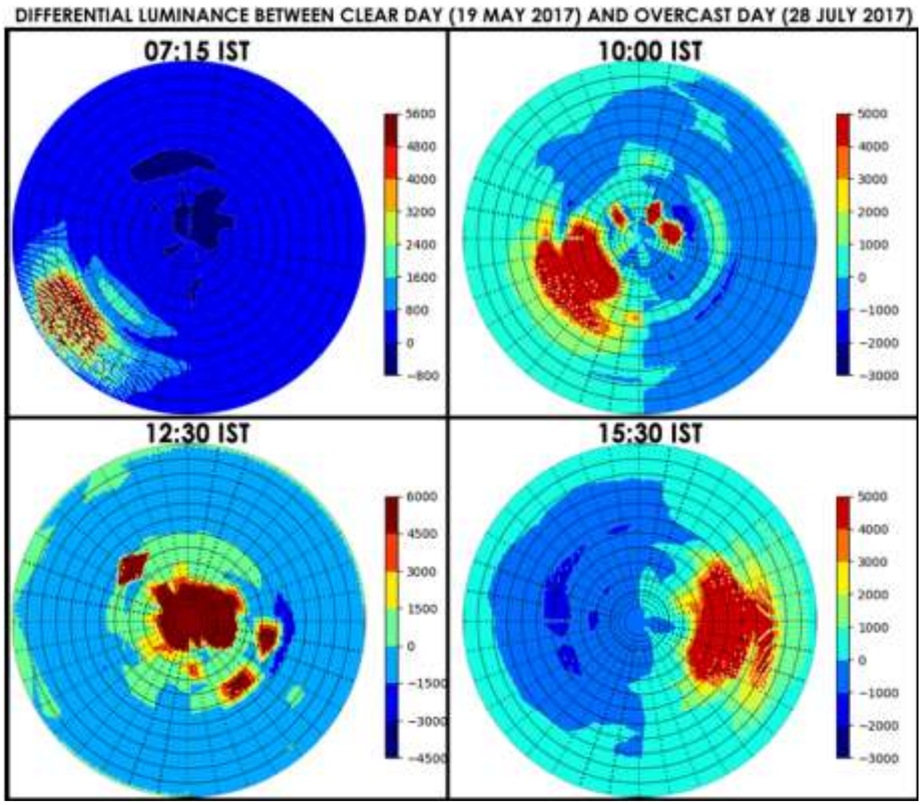

Figure 13: Sky patch luminance difference between a pre-monsoon and a mid-monsoon day for similar declination at various time-points

A positive luminance value was observed for patches closer to Sun-position while a negative value was observed for patches farther away: the luminance of farther patches was higher on an overcast day than on a clear day. Figure 14 demonstrates the altitudinal variation in the differential measured sky luminance between clear and overcast sky at various time. With increase in solar elevation, there is a corresponding peak in differential data from sensor at a specific altitude: 0730h gets a peak at Z+67.5 sensor, 0830-0930h gets a peak at Z+45 sensor, 1000h at Z+30 sensor and so on as demonstrated in Figure 14(a). Moreover, the overall sky luminance on a horizontal plane measured every 15-minutes for clear and overcast days is demonstrated in Figure 14(b).

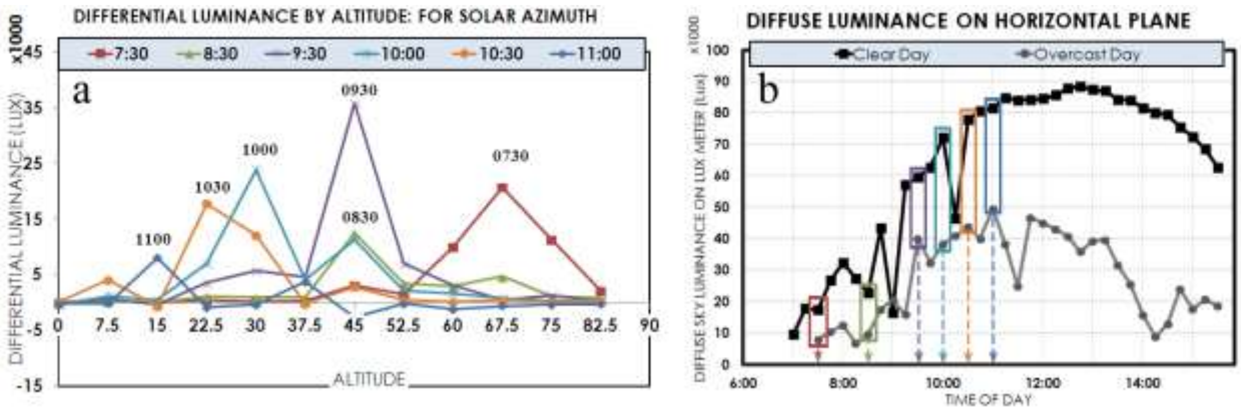

Figure 14: (a) Comparison of luminance between a clear and overcast day with similar Sun path, (b) Global Horizontal Luminance comparison between a clear and overcast day

4. Discussion

This paper presents the design and development of a low cost prototype built at a fraction of the cost of the commercial design. This device aims at capturing the angular luminance of the sky-hemisphere over varying time points. The analytical data captured provides possibilities towards developing sky-maps through data visualization similar to commercial design, or towards further analysis of factors including indoor illuminance and sky-model enhancement. Additionally, Building management systems can possibly make use of the illuminance distribution predictions, and efficiently control electric lights to complement the daylight, dimming and switching off as needed. Through better understanding of ambient sky-types, the simulation programs may be improved towards better indoor simulations, and thus be able to provide better recommendations towards optimal design.

The data measured with our device, when compared with standard sky-models, shows about 20-30% deviation from the closest sky. This could reflect upon the smoothening in the sky models that do not capture intermittent clouds, as well as device sensitivity in the high luminance region: the minimum error count for Arduino is 5V/1024~5mV. The trade-off can thus be considered between cost and accuracy. The differences between our device and the commercially accepted design are summarized in Table 4.

Table 4: Key features and differences between commercial setup and proposed design: concepts and performance analysis post experiment.

	COMMERCIAL	PROPOSED PROTOTYPE	COMMENTS
SKY DIVISIONS	Altitude Bands: 8	Altitude Bands: 12	More bands provide higher smoothening across altitudes.
	Subdivisions: 145/151	Subdivision: 221	Higher data points provides better accuracy
PATCH SIZE	Equal throughout	Widens from zenith towards horizon	Equal patch size helps perform Daylight Coefficient calculations upfront
SENSOR TYPE	Silicon Photodiodes[59] (irradiance & illuminance)	Light Dependent Resistors	Additional irradiance data can be used for Photovoltaic studies and in related fields.
NUMBER OF SENSORS	1+1	12	Single sensor helps uniformity in measurement; multiple sensors can cause discrepancy through calibration
ROTATION	Dual Axis	Vertical, single axis	Dual axis tracking could be additionally complex.
SCAN TIME	4.5 minutes	~2 minutes, may be increased	Slower scanning time can show data discrepancy through distribution, with clouds passing, etc. Faster scanning provides instant snapshot
WEIGHT	12 kg	~10 kg (+/- 2kg)	-
COST	USD 37,500 (2017)	~USD 200	Low cost can help a farther reach: towards a wide network of measurement devices
INTERFACE	Commercial package	Python/ self built. Can be incorporated into further advancements	An open interface for data analysis may be used for various levels of interpretation.
EXPANDABLE	No/commercial	Yes	With advancements, the prototype can be expanded to additional functionalities

5. Conclusions

We present the design, development and validation of a low-cost LDR-based device for measurement of angular daylight luminance distribution. This device was used to capture three distinct seasons: pre-monsoon, mid-monsoon and post-monsoon in Mumbai, India. Light Dependent Resistors were used as sensors owing to their peak sensitivity in the visible light region of the spectrum, thus eliminating the need of costlier sensors like spectral scanners. Our device was able to capture luminance variation on a spatial and temporal basis; and was able to offer repeatable results through an extended period of uninterrupted performance. To counter the accuracy issues with LDRs at higher luminance, exposure control was implemented to reduce direct-Sun exposure. Our low-cost prototype is built using programmable open source Arduino microcontroller, with open data processing algorithms in Python. Through this approach, we were able to produce an angular daylight measurement device with significant accuracy at low cost.

There is a need for measurement based models inculcating the local effects on daylight distribution, and we envision our work towards a wider network of low cost devices periodically measuring and logging the angular sky luminance data onto a repository; thereby improving the accuracy of indoor daylight models for assessing building performance.

Acknowledgement

The first author is grateful to Mr. Gaurav Chawla for the help in fabrication of the device, and during experimentation. Special thanks to Ms Krutika Manjrekar, Mr Manik Konch, Ms Farha Memon and Mr Tanmoy Debnath for their added support. We especially wish to thank Dr Ronita Bardhan for her help.

Funding Sources and additional information

This research did not receive any specific grant from funding agencies in the public, commercial, or not-for-profit sectors. The device described in this paper is filed under Indian Patent Application 201821007607 (pending) filed on 28 Feb 2018.

References

[1] A.K. Jain, A Report on Energy Efficiency and Energy Mix in the Indian Energy System (2030), 2015. https://www.gita.org.in/Attachments/Reports/Energy_Efficiency.pdf (accessed August 10, 2017).

[2] S.K.H. Chow, D.H.W. Li, E.W.M. Lee, J.C. Lam, Analysis and prediction of daylighting and energy performance in atrium spaces using daylight-linked lighting controls, Appl. Energy. 112 (2013) 1016–1024. doi:10.1016/j.apenergy.2012.12.033.

[3] S. Sankhe, I. Vittal, R. Dobbs, A. Mohan, A. Gulati, J. Ablett, S. Gupta, A. Kim, S. Paul, A. Sanghvi, G. Sethy, McKinsey, India's urban awakening : Building inclusive cities , sustaining economic growth, McKinsey Q. (2010) 207.

[4] J.C. Xie, P. Xue, C.M. Mak, J.P. Liu, Balancing energy and daylighting performances for envelope design: A new index and proposition of a case study in Hong Kong, Appl. Energy. 205 (2017) 13–22. doi:10.1016/j.apenergy.2017.07.115.

[5] D.H.W. Li, A review of daylight illuminance determinations and energy implications, Appl. Energy. 87 (2010) 2109–2118. doi:10.1016/j.apenergy.2010.03.004.

[6] I. Acosta, C. Varela, J.F. Molina, J. Navarro, J.J. Sendra, Energy efficiency and lighting design in courtyards and atriums: A predictive method for daylight factors, Appl. Energy. 211 (2018) 1216–1228. doi:10.1016/j.apenergy.2017.11.104.

[7] S. Słomiński, R. Krupiński, Luminance distribution projection method for reducing glare and solving object-floodlighting certification problems, Build. Environ. 134 (2018) 87–101. doi:10.1016/j.buildenv.2018.01.019.

[8] M. Boubekri, J. Lee, A comparison of four daylighting metrics in assessing the daylighting performance of three shading systems, J. Green Build. 12 (2017) 39–53. doi:10.3992/1943-4618.12.3.39.

[9] T.N. Stasinopoulos, A survey of solar envelope properties using solid modelling, J. Green Build. 13 (2018) 3–30. doi:10.3992/1943-4618.13.1.3.

[10] J. Niemasz, J. Sargent, C.F. Reinhart, Solar zoning and energy in detached dwellings, Environ. Plan. B Plan. Des. 40 (2013) 801–813. doi:10.1068/b38055.

[11] E.J. Gago, T. Muneer, M. Knez, H. Köster, Natural light controls and guides in buildings. Energy saving for electrical lighting, reduction of cooling load, Renew. Sustain. Energy Rev. 41 (2015) 1–13. doi:10.1016/j.rser.2014.08.002.

[12] K.K. Chong, N.O. Onubogu, T.K. Yew, C.W. Wong, W.C. Tan, Design and construction of active daylighting system using two-stage non-imaging solar concentrator, Appl. Energy. 207 (2017) 45–60. doi:10.1016/j.apenergy.2017.05.188.

[13] M.S. Mayhoub, D.J. Carter, The costs and benefits of using daylight guidance to light office buildings, Build. Environ. 46 (2011) 698–710. doi:10.1016/j.buildenv.2010.09.014.

[14] A.A. Elmualim, S. Smith, S.B. Riffat, L. Shao, Evaluation of dichroic material for enhancing light pipe/natural ventilation and daylighting in an integrated system, Appl.

Energy. 62 (1999) 253–266. doi:10.1016/S0306-2619(99)00014-8.
[15] S. Aripin, “Healing Architecture”: Daylight in Hospital Design, Sustain. Build. South East Asia. (2007) 5–7.
[16] M. Boubekri, Daylighting, Architecture and Health Building Design Strategies, in: Daylighting, Archit. Heal. Build. Des. Strateg., 2008: p. 92. doi:10.1017/CBO9781107415324.004.
[17] C. Boroff, J. Eickmeier, K. Eklund, C. Garcia, S. Miller, B. Newton, B. Pecka, T. Samuelson, J. Staab, O. Whittaker, Community, campus, and climate at central community college—3C initiative: Kearney center living learning lab and ecosystem, J. Green Build. 13 (2018) 139–156. doi:10.3992/1943-4618.13.1.139.
[18] R. Kittler, S. Darula, Scattered sunlight determining sky luminance patterns, Renew. Sustain. Energy Rev. 62 (2016) 575–584. doi:10.1016/j.rser.2016.05.012.
[19] P. Moon, D. Spencer, Illumination from a non-uniform sky, Trans Illum Eng Soc. 37 (1942) 707–726.
[20] R. Kittler, M. Kocifaj, S. Darula, Daylight Science and Daylight Technology, Springer, New York, 2012.
[21] S. Darula, R. Kittler, CIE General sky standard defining luminance distributions, eSim. (2002) 8.
[22] Autodesk Help, CIE Sky Model | 3ds Max | Autodesk Knowledge Network, (2017). https://knowledge.autodesk.com/support/3ds-max/learn-explore/caas/CloudHelp/cloudhelp/2017/ENU/3DSMax/files/GUID-3636C39D-DAC5-4329-932F-196FDD61AB30-htm.html (accessed April 29, 2018).
[23] M. Inanici, A. Hashemloo, An investigation of the daylighting simulation techniques and sky modeling practices for occupant centric evaluations, Build. Environ. 113 (2017) 220–231. doi:10.1016/j.buildenv.2016.09.022.
[24] A.N.M. Shahriar, Exploration into sky brightness capture through digital camera configuration, in: 44th Annu. Conf. Archit. Sci. Assoc. ANZAScA 2010, 2010.
[25] J. Ramírez-Faz, R. López-Luque, F.J. Casares, Development of synthetic hemispheric projections suitable for assessing the sky view factor on vertical planes, Renew. Energy. 74 (2015) 279–286. doi:10.1016/j.renene.2014.08.025.
[26] F.J. Casares, J. Ramírez-Faz, R. López-Luque, Development of synthetic hemispheric projections suitable for assessing the sky view factor on horizontal planes, Energy Build. 82 (2014) 696–702. doi:10.1016/j.renene.2014.08.025.
[27] E. Ramírez, W.C. Pujols, F.J. Casares, J. Ramírez-Faz, R. López-Luque, Development of a suitable synthetic projection to simultaneously study solar exposure and natural lighting in building windows, Energy Build. 65 (2013) 391–397. doi:10.1016/j.enbuild.2013.06.006.
[28] J.T. Kider, D. Knowlton, J. Newlin, Y.K. Li, D.P. Greenberg, A framework for the experimental comparison of solar and skydome illumination, ACM Trans. Graph. 33 (2014) 1–12. doi:10.1145/2661229.2661259.
[29] L. Komar, A. Rusnak, R. Dubnicka, Analysis of diffuse irradiance from two parts of sky vault divided by solar meridian using portable spectral sky-scanner, Sol. Energy. 96 (2013) 1–9. doi:10.1016/j.solener.2013.07.003.
[30] R. Kittler, Standardisation of the outdoor conditions for the calculation of the Daylight Factor with clear skies, in: Proc. Conf. Sunlight Build., Bouwcentrum Rotterdam, 1967: pp. 273–286.

[31] D.H.W. Li, S. Lou, A. Ghaffarianhoseini, K.A. Alshaibani, J.C. Lam, A review of calculating procedures on daylight factor based metrics under various CIE Standard Skies and obstructed environments, Build. Environ. 112 (2017) 29–44. doi:10.1016/j.buildenv.2016.11.019.
[32] Comission Internationale de L'Eclairage, Spatial distribution of daylight-CIE standard general sky, 2003.
[33] T. Muneer, Solar Radiation and Daylight Models, 2nd ed., Routledge, 2007, 2004. doi:10.1016/B978-075065974-1/50015-2.
[34] V. Ferraro, V. Marinelli, M. Mele, A method for selecting the CIE standard general sky model with regard to calculating luminance distributions, J. Atmos. Solar-Terrestrial Phys. 95–96 (2013) 59–64. doi:10.1016/j.jastp.2013.01.006.
[35] V. Mettanant, P. Chaiwiwatworakul, S. Chirarattananon, A model of Thai's sky luminance distribution based on reduced CIE standard sky types, Renew. Energy. 103 (2017) 739–749. doi:10.1016/j.renene.2016.11.008.
[36] T. Luo, D. Yan, R. Lin, J. Zhao, Sky-luminance distribution in Beijing, Light. Res. Technol. 47 (2015) 349–359. doi:10.1177/1477153514532466.
[37] S.K. Wittkopf, L.K. Soon, Analysing sky luminance scans and predicting frequent sky patterns in Singapore, Light. Res. Technol. 39 (2007) 31–51. doi:10.1177/1365782806070683.
[38] K.A. Alshaibani, Classification Standard Skies: The use of horizontal sky illuminance, Renew. Sustain. Energy Rev. 73 (2017) 387–392. doi:10.1016/j.rser.2017.01.116.
[39] D.H.W. Li, C.C.S. Lau, J.C. Lam, Overcast sky conditions and luminance distribution in Hong Kong, Build. Environ. 39 (2004) 101–108. doi:10.1016/j.buildenv.2003.06.001.
[40] A. Suárez-García, D. Granados-López, D. González-Peña, M. Díez-Mediavilla, C. Alonso-Tristán, Seasonal caracterization of CIE standard sky types above Burgos, northwestern Spain, Sol. Energy. 169 (2018) 24–33. doi:10.1016/j.solener.2018.04.028.
[41] D.H.W. Li, S. Lou, J.C. Lam, R.H.T. Wu, Determining solar irradiance on inclined planes from classified CIE (International Commission on Illumination) standard skies, Energy. 101 (2016) 462–470. doi:10.1016/j.energy.2016.02.054.
[42] S. Lou, D.H.W. Li, J.C. Lam, E.W.M. Lee, Estimation of obstructed vertical solar irradiation under the 15 CIE Standard Skies, Build. Environ. 103 (2016) 123–133. doi:10.1016/j.buildenv.2016.04.005.
[43] D.H.W. Li, G.H.W. Cheung, K.L. Cheung, T.N.T. Lam, Determination of vertical daylight illuminance under non-overcast sky conditions, Build. Environ. 45 (2010) 498–508. doi:10.1016/j.buildenv.2009.07.008.
[44] H. Xiao, Q. Kang, J. Zhao, Y. shi Xiao, A dynamic sky recognition method for use in energy efficient lighting design based on CIE standard general skies, Build. Environ. 45 (2010) 1319–1328. doi:10.1016/j.buildenv.2009.11.014.
[45] S. Lou, D.H.W. Li, J.C. Lam, CIE Standard Sky classification by accessible climatic indices, Renew. Energy. 113 (2017) 347–356. doi:10.1016/j.renene.2017.06.013.
[46] M. Spitschan, G.K. Aguirre, D.H. Brainard, A.M. Sweeney, Variation of outdoor illumination as a function of solar elevation and light pollution, Sci. Rep. 6 (2016). doi:10.1038/srep26756.
[47] M. de Simón-Martín, C. Alonso-Tristán, D. González-Peña, M. Díez-Mediavilla, New device for the simultaneous measurement of diffuse solar irradiance on several azimuth and tilting angles, Sol. Energy. 119 (2015) 370–382. doi:10.1016/j.solener.2015.06.001.

[48] Y.S. Chiou, P.C. Huang, An HDRi-based data acquisition system for the exterior luminous environment in the daylight simulation model, Sol. Energy. 111 (2015) 104–117. doi:10.1016/j.solener.2014.10.032.
[49] R. Chauvin, J. Nou, S. Thil, S. Grieu, Modelling the clear-sky intensity distribution using a sky imager, Sol. Energy. 119 (2015) 1–17. doi:10.1016/j.solener.2015.06.026.
[50] D.H.W. Li, E.K.W. Tsang, An analysis of measured and simulated daylight illuminance and lighting savings in a daylit corridor, Build. Environ. 40 (2005) 973–982. doi:10.1016/j.buildenv.2004.09.007.
[51] D. Li, C. Lau, J. Lam, Predicting daylight illuminance by computer simulation techniques, Light. Res. Technol. 36 (2004) 113–129. doi:10.1191/1365782804li108oa.
[52] D.H.W. Li, C.C.S. Lau, J.C. Lam, Evaluation of overcast-sky luminance models against measured Hong Kong data, Appl. Energy. 70 (2001) 321–331. doi:10.1016/S0306-2619(01)00044-7.
[53] D.H.W. Li, J.C. Lam, C.C.S. Lau, A Study of Solar Radiation Daylight Illuminance and Sky Luminance Data Measurements for Hong Kong, Archit. Sci. Rev. 45 (2002) 21–30. doi:10.1080/00038628.2002.9696932.
[54] M.T. Markou, A. Bartzokas, H.D. Kambezidis, A new statistical methodology for classification of sky luminance distributions based on scan data, Atmos. Res. 86 (2007) 261–277. doi:10.1016/j.atmosres.2007.06.001.
[55] P. Ineichen, B. Molineaux, R. Perez, Sky luminance data validation: Comparison of seven models with four data banks, Sol. Energy. 52 (1994) 337–346. doi:10.1016/0038-092X(94)90140-6.
[56] P.R. Tregenza, Subdivision of the sky hemisphere for luminance measurements, Light. Res. Technol. 19 (1987) 13–14. doi:10.1177/096032718701900103.
[57] L. Kómar, M. Kocifaj, Uncertainty of daylight illuminance on vertical building façades when determined from sky scanner data: A numerical study, Sol. Energy. 110 (2014) 15–21. doi:10.1016/j.solener.2014.09.010.
[58] F. Ciampini, P.S. Scarazzato, A.A.R. Neves, D.C.L. Pereira, M.H. Yamanaka, Low cost data acquisition module for evaluating the quantitative performance of daylight systems, Sol. Energy. 81 (2007) 1187–1190. doi:10.1016/j.solener.2007.01.013.
[59] J.L. Torres, L.M. Torres, Angular Distribution of Sky Diffuse Radiance and Luminance, in: V. Badescu (Ed.), Model. Sol. Radiat. Earth's Surf. Recent Adv., Springer, Berlin, 2008: p. 444. https://books.google.co.in/books?id=N8kI8k-ED18C (accessed April 29, 2018).